FINITE ELEMENT ANALYSIS OF OFFSHORE MONOPILE FOUNDATIONS

Influence of Fault Discontinuity Offset, Dip, and Load Orientation

Muhammad Mohsan, Bruno Stuyts
OWI Lab, Vrije Universiteit Brussel, Belgium

Contents

Abstract

Offshore monopile foundations are widely used to support wind turbines, often in complex seabed conditions. However, natural geological features, such as fold and fault zones, can significantly alter monopile behavior by reducing soil stiffness and introducing preferential slip planes. Observations of faulted clay layers (Kortrijk Formation) in the Princess Elisabeth Zone (PEZ) offshore Belgium have brought the issue of foundation–fault interaction to the attention of researchers (Saritas et al., 2025). In the Claytectonics research project, these faults have been surveyed with seismic methods and a mapping of the faults was carried out in several pseudo-3D blocks. This allowed the researchers to map out the faults and identify their geometrical properties.

This study investigates the influence of fault offset, dip angle, and lateral load orientation on monopile response using a series of parametric three-dimensional finite element simulations. A systematic matrix of one hundred and fifty-three (153) numerical experiments was conducted, in which the monopile position relative to the fault, the inclination of the fault plane, and the direction of applied lateral loading were varied independently. In the numerical model, the fault was introduced as a plane with strength properties which are different from the surrounding soil mass. The monopile response was evaluated in terms of lateral displacement profiles, bending moment distributions along the pile length, and mudline stiffness.

The results demonstrate that monopile behavior is highly sensitive to proximity to the fault. Small offsets (0–10 m) lead to pronounced increases in pile-head displacement and a substantial reduction in mudline stiffness, while the influence of the fault diminishes progressively with increasing offset and becomes negligible at offsets of approximately 25 m. The response is asymmetric, with configurations corresponding to positive (hanging-wall) offsets exhibiting a stronger degradation in stiffness than negative (footwall) offsets.

The dip angle of the fault is shown to play a secondary role at large offsets but becomes critical when the monopile is located close to the fault. For offsets of 1–5 m, mid- to steeply dipping discontinuities induce the most adverse response, with dip angles in the range of approximately 60°–70° identified as particularly critical. In addition, the orientation of lateral loading relative to the fault strongly affects the monopile response at small offsets, with fault-normal loading producing the largest displacements and bending moments due to enhanced normal interaction with the weak plane.

Overall, the study highlights the importance of explicitly accounting for fault geometry and load alignment in the design and assessment of offshore monopile foundations in faulted clay seabeds. The findings provide practical guidance on when simplified intact-ground assumptions may be unconservative and underline

the need for advanced numerical modelling in geologically complex offshore environments.

1 Introduction

Monopile foundations support more than 80% (Kallehave et al., 2015; WindEurope, 2021) of offshore wind turbines worldwide due to their structural simplicity and cost efficiency. Conventional design typically assumes homogeneous soil conditions, yet offshore sites often exhibit heterogeneities such as weak layers, discontinuities, or faults. Geophysical surveys in the Princess Elisabeth Zone offshore Belgium have revealed large-scale faulting with different spacing, strike and dip (Andikagumi et al., 2025; Henriet et al., 1988). These features may significantly influence the soil-pile interaction mechanism as faults often introduce weaker planes in the sediment, which may modify stress transfer and bending response. This study aims to systematically assess the impact of the following factors on monopile performance.

- Fault offset from the monopile centreline,
- Fault plane dip angle, and
- Applied lateral load orientation relative to the strike of the faults,

Finite element analyses were carried out in PLAXIS 3D, with results presented in terms of monopile displacement profiles and bending moment profiles.

2 Methodology

2.1 Modelling approach

The three-dimensional finite element model was developed in PLAXIS 3D with carefully selected domain extents to avoid boundary interference with the pile–soil–fault interaction mechanisms. The model extends from x = -100 m to x = +40 m in the longitudinal direction and from y = -40 m to y = +40 m in the transverse direction, while the vertical extent reaches a depth of 50 m below ground level (¿10m deeper than the planned monopile penetrations). The increased extent on the left-hand side ensures that the lower termination of the inclined fault does not interact with the lateral boundary as the fault plane progressively migrates leftwards during offset simulations. The bottom boundary is placed sufficiently deep to remain outside the zone of significant stress influence.

The soil and fault properties adopted in the analyses are carefully determined on the basis of laboratory testing and site specific characterization (Fugro, 2024; Stuyts et al.,

2025), ensuring that the input parameters accurately reflect the physical behavior of the system. These properties are summarized in Table 1 for the intact soil material and Table 2 for the fault. While the intact soil was modeled undrained (because of the very low permeability of the intact material), the choice was made to model the discontinuities in a drained manner. For a monopile pushing a passive wedge ahead of itself during quasi-static thrust loading from the wind turbine rotor, the existence of a fault plane extending to the seabed or into permeable layers could lead to the creating of drainage paths. Modelling the faults with drained properties is deemed conservative.

Table 1: Material properties of the soil layer

Property	**Name**	**OC Clay**	**Unit**
General			
Soil model	Model	Mohr-Coulomb	-
Drainage type	Type	Undrained C	-
Unsaturated unit weight	γ_{unsat}	17.0	kN/m^3
Saturated unit weight	γ_{sat}	17.0	kN/m^3
Mechanical			
Young's modulus	E'_{ref}	$75 \cdot 10^3$	kN/m^2
Poisson's ratio	ν	0.495	-
Undrained shear strength	$s_{u,ref}$	150	kN/m^2
Increase in undrained shear strength	$s_{u,inc}$	3.75	kN/m^2/m

Table 2: Material properties of fault

General			
Material model	Mohr–Coulomb		
Drainage type	Drained		
Mechanical			
Normal stiffness	k_n	1.0×10^6	kN/m^3
Shear stiffness	k_s	1000	kN/m^3
Cohesion	c'	0.10	kN/m^2
Friction angle	φ'	14.0	°
Dilatancy angle	ψ	0.0	°

The monopile is modelled as a beam element, allowing efficient representation of its axial and flexural response while capturing soil–structure interaction through embedded beam theory without full three-dimensional solid discretisation. The geometric and mechanical properties of the monopile are provided in Table 3.

Table 3: Material properties of monopile for a typical 9MW support structure (from confidential design documentation)

Property	**Name**	**Monopile**	**Unit**
General			
Soil model	Model	Elastic	-
Unit weight	γ	61.5	kN/m^3
Mechanical			
Cross section type	Predefined	Circular tube	-
Diameter	D	8.0	m
Thickness	t	0.10	m
Cross sectional area	A	2.482	m^2
Second moment of area	I_2	19.36	m^4
Second moment of area	I_3	19.36	m^4
Young's modulus	E	210.0×10^6	kN/m^2

A non-uniform mesh is adopted, with local refinement applied around the monopile, the soil–pile interface, and the fault where high stress and strain gradients are expected. The mesh is gradually coarsened towards the far-field boundaries to reduce computational cost. Mesh sensitivity checks confirm that further refinement has a negligible influence on the global response and key output parameters, indicating mesh-independent results. The locally refined mesh in the vicinity of the monopile and the fault is illustrated in Fig.1.

The staged construction analysis has been conducted using three sequential calculation phases. In the initial phase, the in-situ stress state has been established using the K_0-procedure, whereby geostatic equilibrium has been achieved through gravity loading while enforcing the prescribed at-rest earth pressure coefficient. The first calculation phase initiates the model. The fault is already included in the model during this first calculation phase. The installation of the monopile is not simulated, it is entered in the model as a *wished-in-place* geometrical feature. The first calculation phase brings the model into equilibrium with the pre-existing stress field. This phase captures the stress redistribution and stiffness modification associated with the presence of both fault and pile. In the second phase, lateral loading is applied at the monopile head in the form of a combined horizontal force and bending moment, representing operational loading conditions. The resulting structural response is evaluated in terms of lateral displacement and bending moment distributions along the monopile.

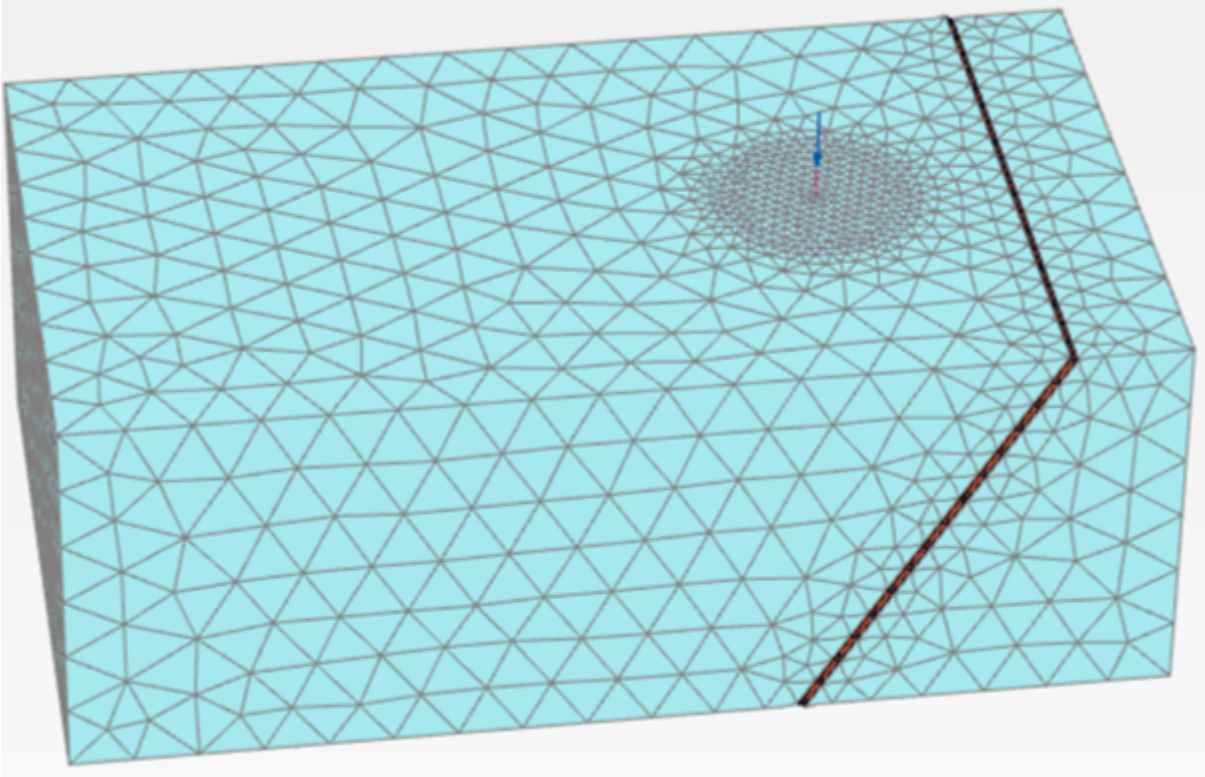

(a) Global connectivity plot with mesh refinement around the monopile and fault

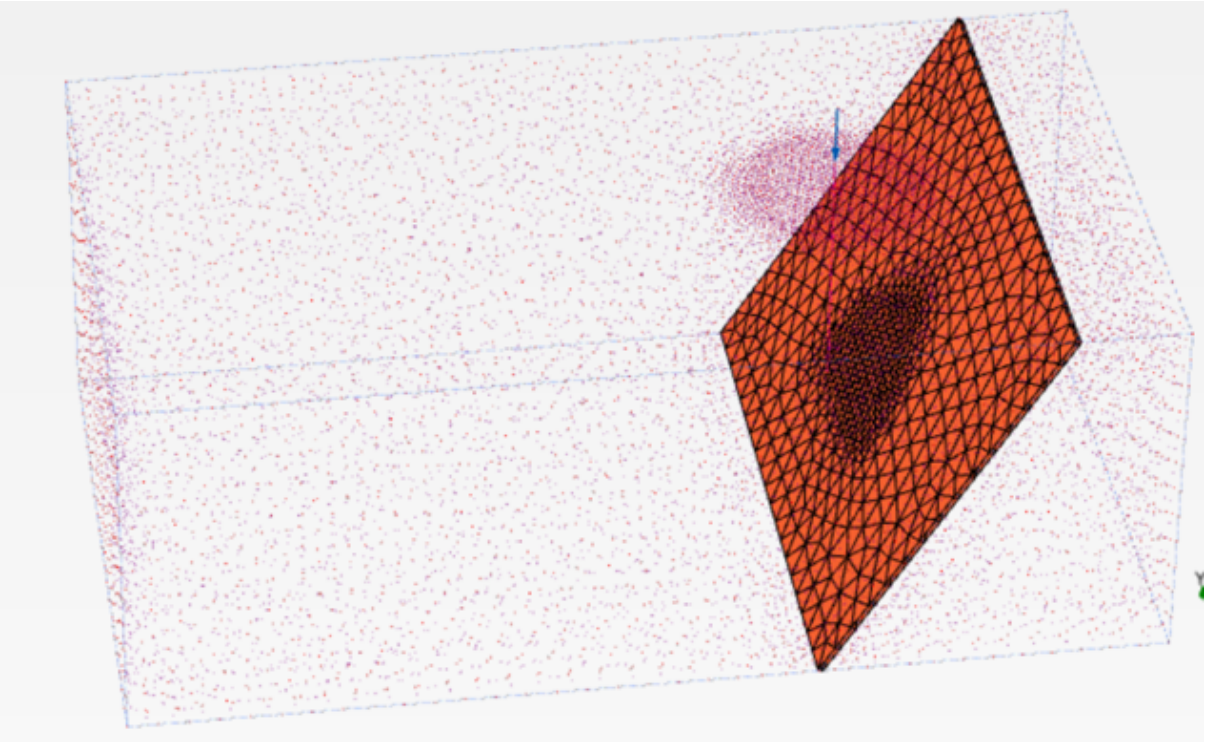

(b) Global view with distribution of nodes and stress points

Figure 1: FEM mesh overview

2.2 Pile response analysis for intact soil

The reference numerical model represents an offshore monopile embedded in a fully intact and laterally continuous soil mass, established to define baseline behavior prior to introducing any geological fault. The soil domain is assumed continuous in all directions, ensuring uniform stiffness and strength around the pile and allowing pile–soil interaction to develop without kinematic incompatibilities or stress localization. The monopile is modelled as a beam element with constant axial and bending stiffness along its 30 m embedded length below the mudline, enabling reliable evaluation of lateral displacement and bending moment profiles.

A static point load is applied at the pile head to represent operational lateral loading, consisting of a horizontal force of 100 kN in the global x-direction combined with an overturning moment of 10,000 kN·m about the global y-axis. This loading configuration induces lateral pile deflection and a smooth bending moment distribution along the embedded length, with soil resistance mobilized progressively through shaft–soil interaction.

The FEM model results are expressed as lateral displacement and bending moment distributions along the embedded pile length, together with a mudline stiffness term, defined as $k_{\text{mud}} = M/U_x$ at the mudline. Fig. 2 shows the baseline response of the monopile in intact clay. The lateral displacement profile (Ux) decreases smoothly with depth, with maximum displacement at the pile head and progressive mobilization of soil resistance along the shaft, resulting in a smaller movement near the pile toe. The absence of irregularities indicates uniform pile–soil interaction and continuous ground conditions. The bending moment profile (M) exhibits a typical monopile response, with the maximum moment developing close to the mudline and gradually reducing with depth as lateral soil reactions increase. The smooth and continuous shape of both profiles confirms stable load transfer without stress or deformation localization.

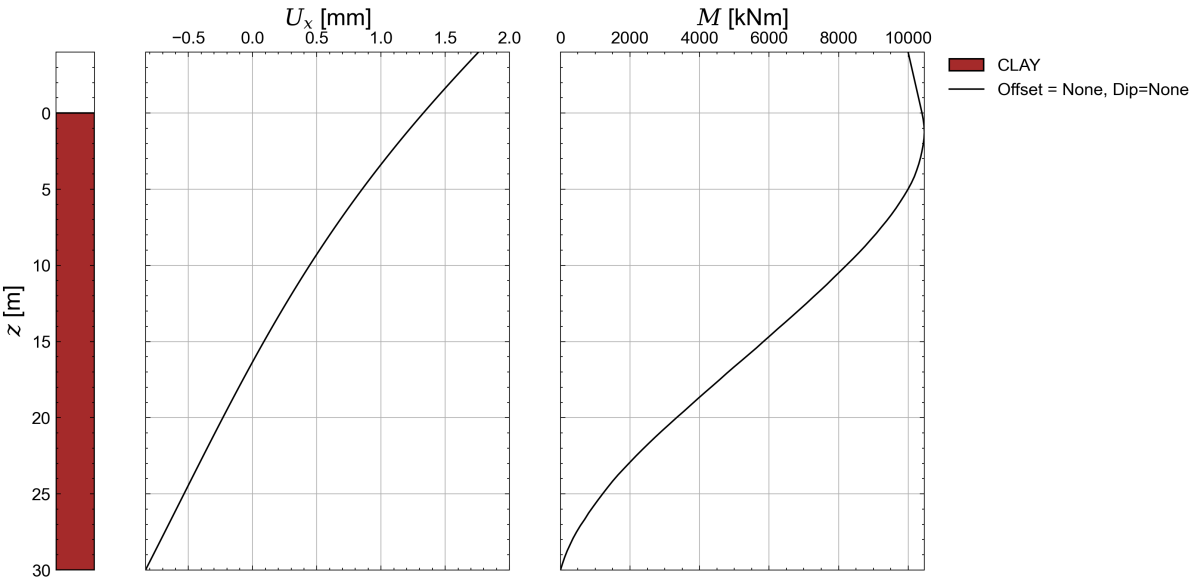

Figure 2: Lateral displacement (U_x) and bending moment (M) profiles along the monopile depth (reference model: no fault offset, no fault dip).

Fig. 3 shows the reference mudline stiffness of the monopile for the intact ground condition, with no fault offset and no fault dip. The mudline stiffness is approximately $K_{\text{mud}} \approx 7.84 \times 10^6\,\text{kN/m}$. This value therefore defines the baseline mudline stiffness, against which any changes observed in faulted cases can be evaluated to derive the mechanical influence of the geological fault.

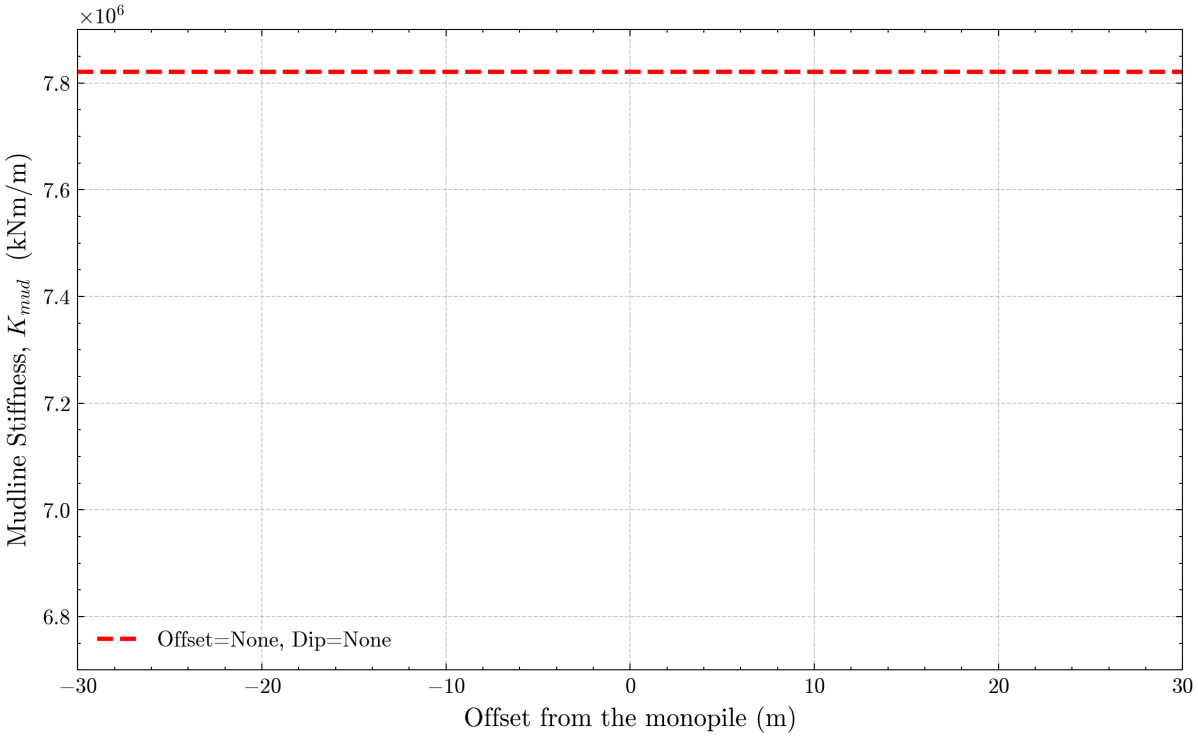

Figure 3: Mudline stiffness K_{mud} for the monopile in intact soil

These results define the reference behavior, providing a benchmark for assessing displacement and bending moment amplification in models incorporating fault offset and dip.

3 Design of Experiment

The intact-ground model serves as the control case for the parametric investigation of fault offset and dip effects. The geophysical surveys showed variable fault spacing, strike and dip (Andikagumi et al., 2025). To capture the influence of fault–monopile interaction under different geological and loading scenarios, a structured parametric experimental matrix has been developed. In total, one hundred and fifty four (154) simulations have been executed to cover all parameter combinations in a consistent and systematic manner. The design of the experimental matrix ensured that the isolated effects of offset, dip, and load orientation could be separately identified while maintaining a logical progression across the parametric space. The complete list of experiments has been added in Appendix A. The design of the experiments has been guided by three principal objectives:

3.1 Effect of offset of fault to monopile

The first series of simulations has investigated the role of positive and negative offsets between the monopile and the fault. The offset is measured between the center of the pile and the fault as it appears at the seabed. Offsets ranging from +25 m (monopile located on the hanging-wall side) to -25 m (monopile located on the footwall side) have been applied, including intermediate and near-fault positions down to sub-meter distances, while a constant average fault dip of 57° has been maintained based on the mean dip derived from geophysical surveys. The maximum offsets were determined in an iterative manner. Exploratory analysis indicated that for +25m and -25m offsets, the interaction of the monopile with the fault became limited. For all offset configurations, identical operational loading conditions have been imposed, consisting of a horizontal load applied in the x-direction and a prescribed bending moment at the pile head. This parametric framework has enabled a systematic assessment of how the relative position of the monopile with respect to the fault has governed lateral displacement, bending moment distribution, and mudline stiffness, thereby isolating the effect of offset from other geometrical and loading influences. Fig. 4 illustrates representative model configurations with the fault located at two different offset distances.

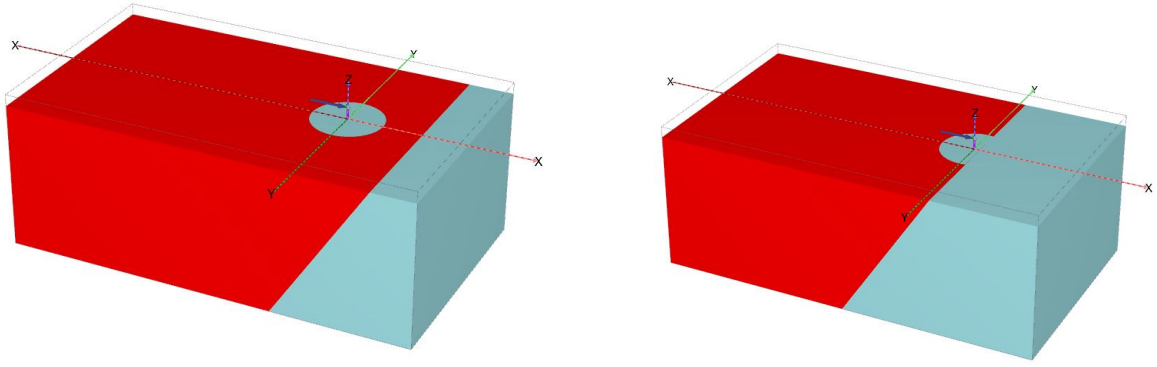

(a) fault at offset = 25 m (b) fault at offset = 2 m

Figure 4: Model scenarios illustrating monopile–fault configurations at different offset distances.

3.2 Effect of dip of fault

The second set of experiments focused on the influence of the fault dip angle. The dip sensitivity analysis was performed by systematically varying the fault dip angle at multiple fixed monopile–fault offset positions. Offsets were reduced stepwise from 25 m to 1 m relative to the fault centreline, representing increasing proximity of the monopile to the fault zone. For each selected offset, a consistent set of dip angles ranging from 70° (steep) to 35° (shallow) is applied in accordance with the range reported by Andikagumi and Batist (2025), while maintaining identical loading conditions across all simulations. This experimental design ensures that the influence of fault dip is evaluated independently at each offset position, enabling a clear assessment of how fault inclination governs lateral displacement, bending moment, and mudline stiffness in the monopile–soil system as the monopile approaches the fault. Fig. 5 illustrates representative model configurations with the fault located at two different dips.

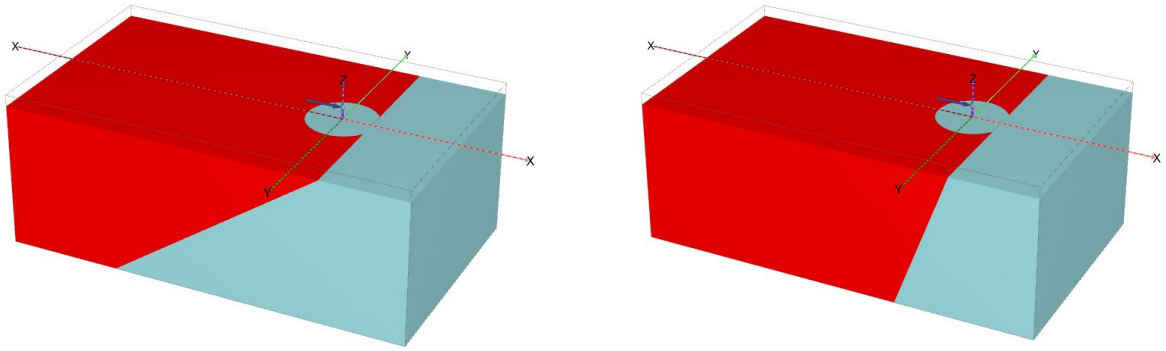

(a) Dip = 35° (b) Dip = 70°

Figure 5: Model scenarios illustrating monopile–fault configurations for different fault dip angles.

3.3 Effect of load orientation relative to fault strike

In the third set of experiments, the influence of loading direction relative to the fault is investigated while maintaining the same fault offset and dip configurations. The monopile–fault offset is reduced stepwise from 10 m to 1 m, and the fault dip angle is varied between 35° and 70°, while the magnitude of the applied loads is kept constant across all simulations.

The loading direction is varied by applying different combinations of horizontal forces (F_x, F_y) and bending moments (M_x, M_y) to represent lateral loading oriented perpendicular, parallel, and oblique to the fault for a given offset and dip of fault. Loading perpendicular to the fault is modelled using $F_x = 100$ kN with a corresponding bending moment $M_y = 10{,}000$ kN·m, representing maximum normal interaction with the weak plane. Loading parallel to the fault is applied using $F_y = 100$ kN and $M_x = 10{,}000$ kN·m, minimising direct normal interaction with the fault. Oblique loading conditions are introduced at 30° and 60° relative to the fault by decomposing the lateral load into combined force and moment components. For the 30° case, $F_x = 86.6$ kN and $F_y = 50$ kN are applied with corresponding moments $M_y = 8{,}660$ kN·m and $M_x = 5{,}000$ kN·m, while for the 60° case the force and moment components are reversed ($F_x = 50$ kN, $F_y = 86.6$ kN; $M_y = 5{,}000$ kN·m, $M_x = 8{,}660$ kN·m). Vertical forces and torsional moments (F_z, M_z) are set to zero in all cases to isolate lateral response. Fig. 6 illustrates representative model configurations for different loading orientations applied relative to the geological fault.

By keeping the load magnitude constant and varying only its orientation, this experimental design enables a clear assessment of how loading direction relative to a geological fault, in combination with fault dip and offset, governs lateral displacement, bending

moment distribution, and mudline stiffness of the monopile–soil system. The results are presented in the following way.

$$U = U_x \cos\theta - U_y \sin\theta \tag{1}$$

$$M = \sqrt{M_x^2 + M_y^2} \tag{2}$$

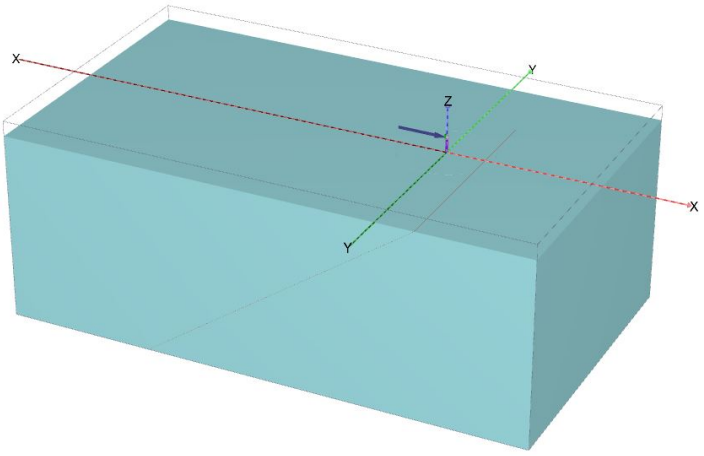

(a) Perpendicular loading (90°)

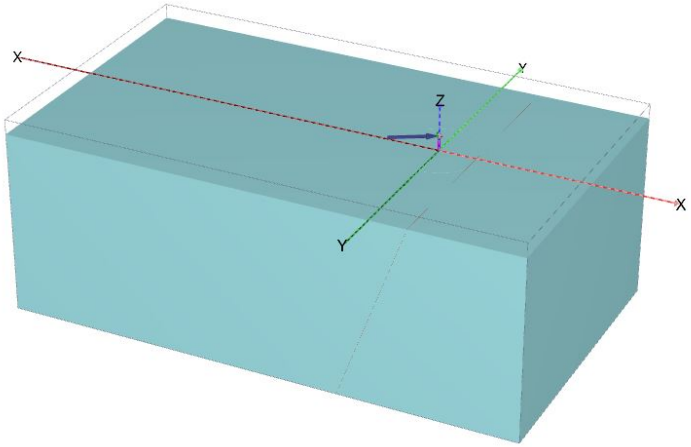

(b) Oblique loading (30°)

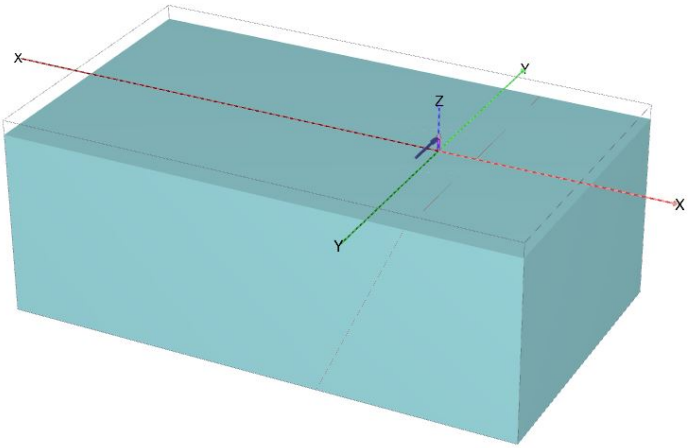

(c) Parallel loading (0°)

Figure 6: Schematic illustration of loading orientations applied relative to the geological fault: perpendicular (90°), oblique (30°), and parallel (0°) loading conditions.

4 Results and Discussion

The analyses are expected to provide the following key outputs, which characterise the monopile response and soil behaviour:

1. Pile lateral displacement profile along the depth
2. Bending moment profile along the pile depth
3. Mudline stiffness

4.1 Effect of Fault Offset

In this section, the results of the fault offset analysis are presented in the form of lateral displacement profiles along the pile, bending moment distributions, and mudline stiffness. The mudline stiffness is evaluated as the ratio of the bending moment to the corresponding lateral displacement at the mudline, defined as $k_{\text{mud}} = M/U_x$. The fault distance is varied from +25 m (monopile located on the hanging-wall side) to -25 m (monopile located on the footwall side), while a constant average fault dip of 57° is maintained.

Fig. 7 presents the lateral displacement profiles along the monopile and the corresponding bending moment distributions for different positive monopile–fault offsets at a constant fault dip of 57°. The response of the monopile in intact ground conditions, represented by the no-fault case, is included as a reference baseline.

In the reference configuration, the monopile exhibits a smooth lateral displacement profile with maximum displacement at the pile head and a corresponding bending moment that increases towards the mudline. As the monopile approaches the fault, deviations from this baseline become apparent. For very small offsets of 0.1 m and 2 m, the pile head displacement increases significantly compared to the no-fault case, with elevated displacements observed over the upper portion of the pile. These changes are accompanied by noticeable modifications in the bending moment distribution, reflecting a reduction in lateral stiffness and confinement due to direct interaction with the faulted material. The presence of the fault influences the failure mechanism with part of the load being transferred to the fault, which has less capacity to absorb it, compared to the intact soil.

At intermediate offsets between 5 m to 15 m, the influence of the fault remains evident but gradually diminishes with increasing distance. The displacement profiles show moderate increases relative to the intact case, indicating a transitional response in which the monopile is partially affected by the fault while still benefiting from the stiffness of the surrounding intact soil.

For larger offsets i.e. 25 m, both the lateral displacement and bending moment profiles closely match those of the no-fault case. The near overlap of the curves indicates that, at

these distances, the mechanical influence of the fault becomes negligible and the monopile response is governed primarily by far-field soil properties.

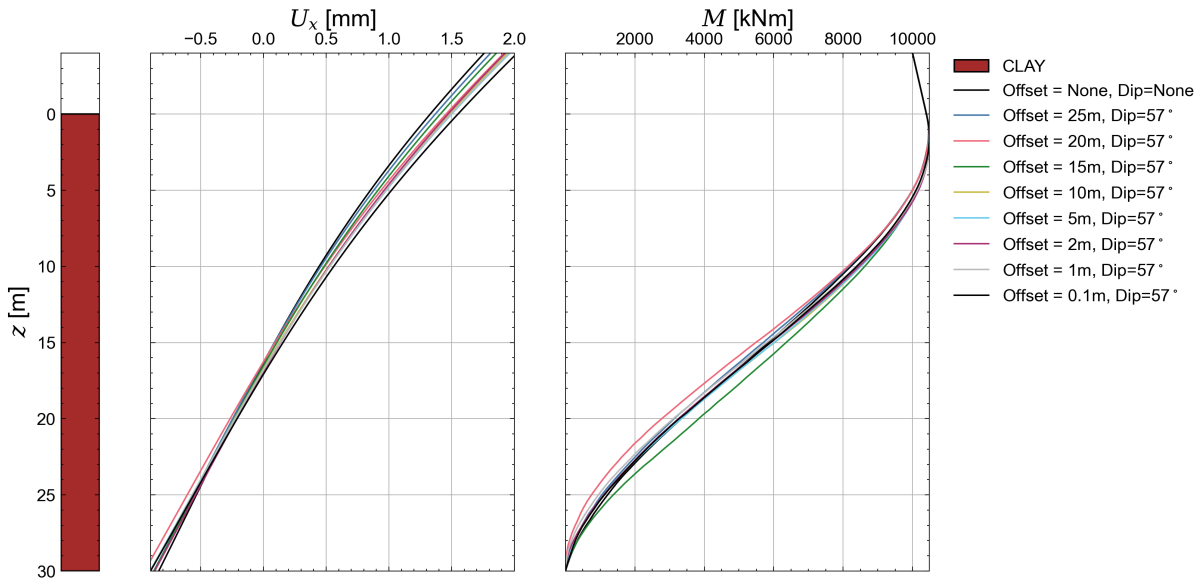

Figure 7: Variation of lateral displacement (U_x) and bending moment (M) with depth for different positive offsets of the fault (Dip = 57°).

Fig. 8 summarizes the monopile response for a range of negative offsets (footwall side). Overall, the monopile response for negative offsets shows limited deviation from the reference case, with lateral displacement and bending moment profiles remaining closely clustered across all considered distances from the fault. The greatest changes in the lateral displacement profile are observed for those offsets very close to the fault (-2 m and -5 m), where an increase in pile head displacement can be identified.

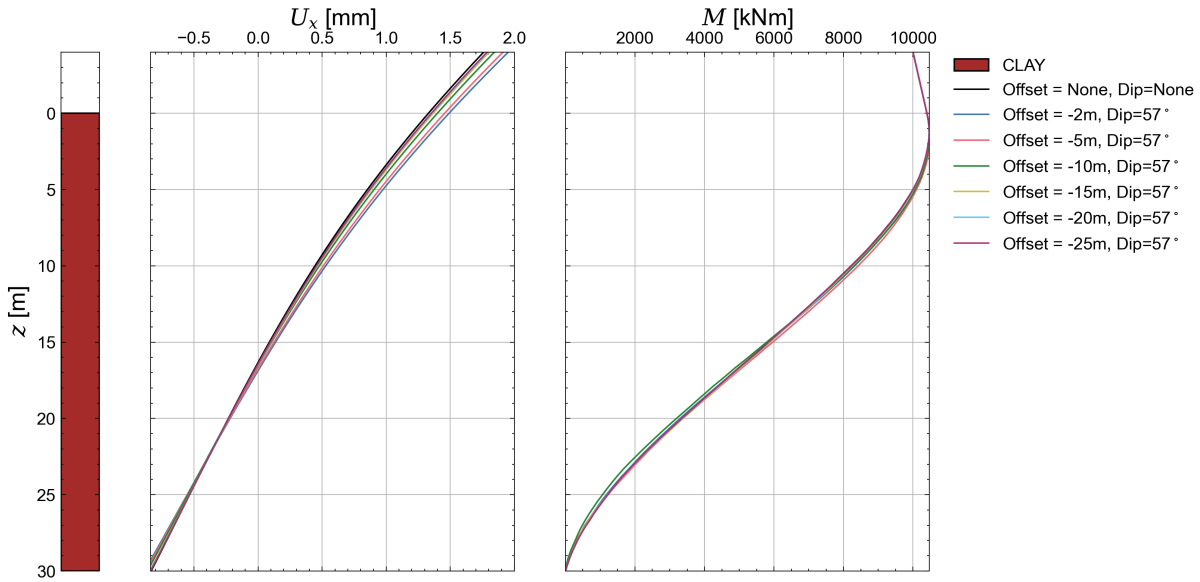

Figure 8: Variation of lateral displacement (U_x) and bending moment (M) with depth for different negative offsets of the fault (Dip = 57°).

To summarise the results for all offset configurations, the mudline stiffness , as shown in Fig. 9, is computed to assess the extent to which the presence of a fault degrades the lateral stiffness of the monopile system. The intact case provides the upper bound of stiffness, whereas all fault scenarios lead to a measurable reduction in mudline stiffness. The positive offsets exhibit significant reductions in mudline stiffness when the pile is positioned near the fault. The most pronounced reduction is observed when the fault intersects the pile axis (offset= 0.1 m), indicating a strong localisation of deformation and reduced soil–pile interaction efficiency. Negative offset configurations demonstrate a more restrained response, indicating a comparatively stiffer and more stable soil–pile interaction on the side of the footwall of the fault.

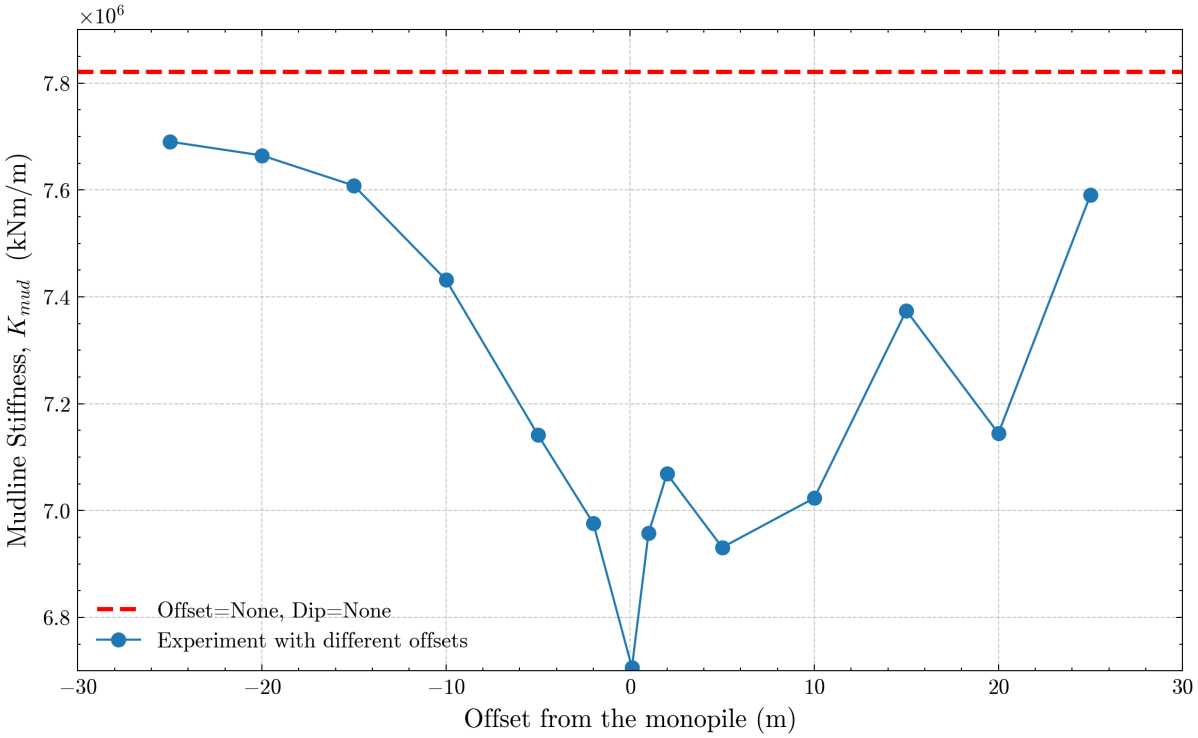

Figure 9: Mudline stifness ($k_{\text{mud}} = M/U_x$)for different offsets of the fault (Dip = 57°).

Figure 10 presents the lateral displacement (U_x) contours for two representative cases with the fault located at offsets of 2 m and 25 m from the monopile. The comparison highlights a clear change in the spatial distribution of lateral displacements as the fault approaches the pile. For the offset = 2 m case, the U_x contours exhibit a distinctly non-symmetric deformation pattern, with strongly localised displacement gradients developing near the pile and along the fault. The deformation field is biased towards the weak plane, indicating direct interaction, reduced lateral confinement, and stiffness degradation.

In contrast, for offset = 25 m case, shows a largely symmetric and smoothly distributed displacement field, with deformations confined to the vicinity of the pile and negligible influence from the distant fault. This symmetry indicates that the response is governed

primarily by the intact soil mass.

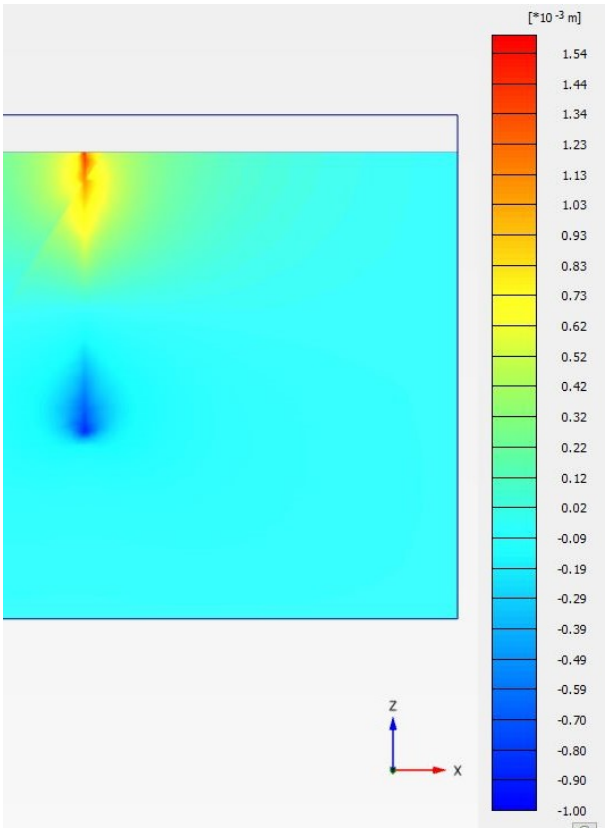

(a) U_x contour for near-field fault (offset = 2 m).

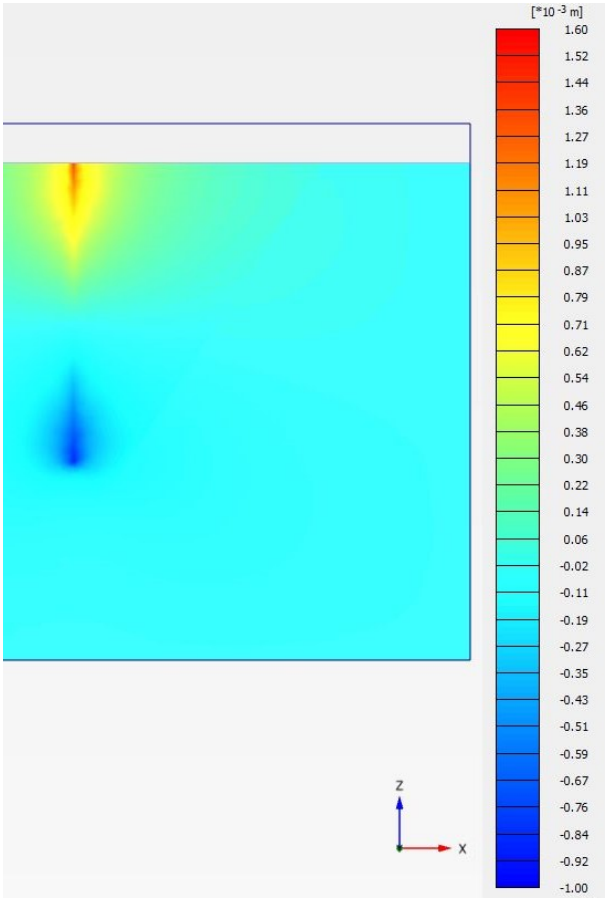

(b) U_x contour for far-field fault (offset = 25 m).

Figure 10: Comparison of lateral displacement (U_x) contours for offset=2m and offset=25m fault configurations.

4.2 Effect of Fault Dip

In these sets of results, the dip angle of the fault has been varied systematically, ranging from 35° to 70° following Andikagumi et al. (2025), in order to investigate the influence of fault inclination on the lateral response of the monopile. Varying the dip angle alters the orientation of the weak plane relative to the pile axis and the direction of applied loading, thereby influencing the stress transfer mechanisms and soil–pile interaction. The offsets considered in this analysis, namely 1 m, 2 m, 5 m, 10 m, and 25 m, correspond to the range identified from geophysical surveys.

Fig. 11 presents the lateral displacement and bending moment profiles for a fault located at an offset of 25 m from the monopile, for dip angles ranging from 35° to 70°. At this large offset, the influence of the fault on the monopile response is minimal. Both the displacement and bending moment profiles closely follow the intact reference case, with only marginal deviations observed near the mudline, especially for the dip 35°.

Taken together, Fig. 12 to 15 show a clear change in behavior from an almost intact response at large offsets to a response strongly influenced by the fault at small offsets. As the fault moves closer to the monopile, lateral displacements increase and bending moments decrease, indicating a gradual reduction in mudline stiffness. At large offsets, the dip angle has only a minor effect on the monopile response. However, at smaller offsets, the influence of dip angle becomes more pronounced, as the orientation of the weak plane controls the deformation pattern and load transfer. Overall, the results demonstrate that both the distance to the fault and its inclination play a role in monopile lateral behavior. This is further examined by plotting the monopile lateral stiffness against the fault dip for the various offsets.

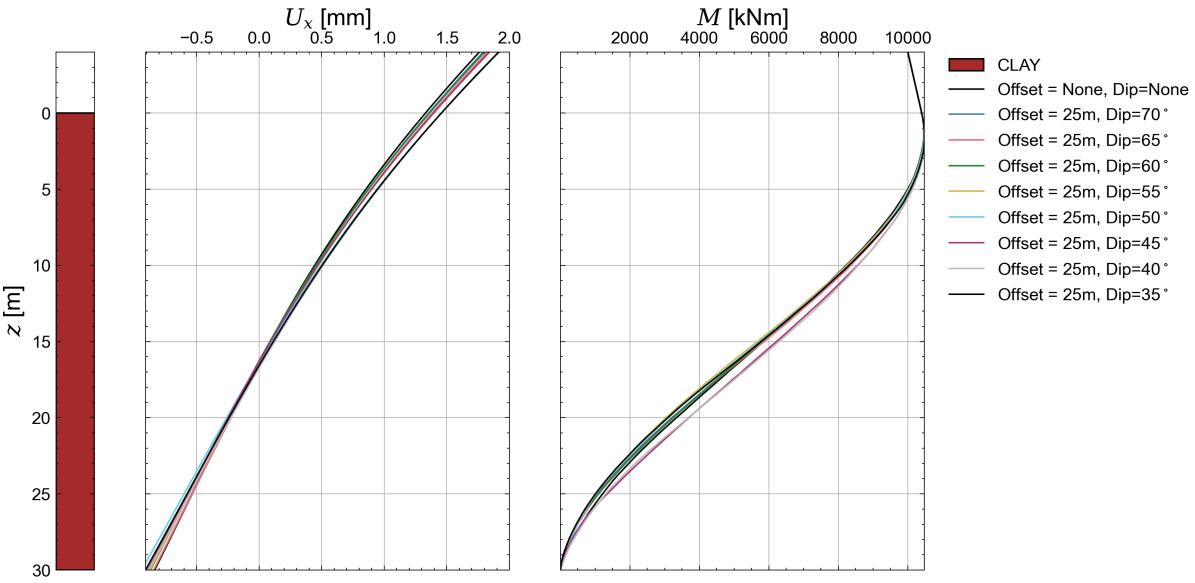

Figure 11: Variation of lateral displacement (U_x) and bending moment (M) with depth for different dips at of the fault (offset = 25 m).

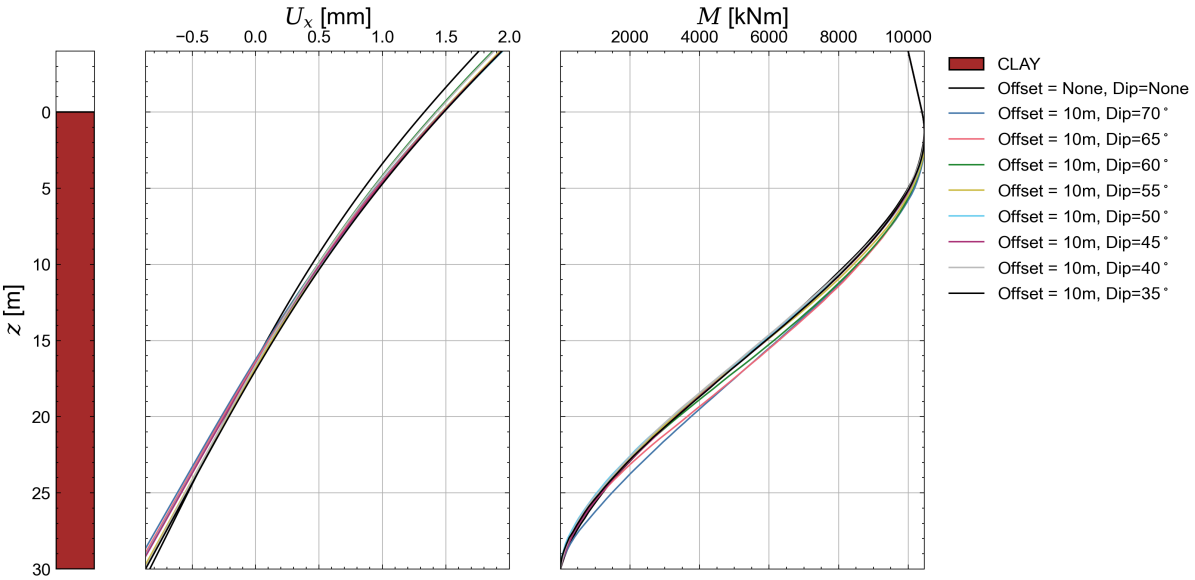

Figure 12: Variation of lateral displacement (U_x) and bending moment (M) with depth for different dips at of the fault (offset = 10 m).

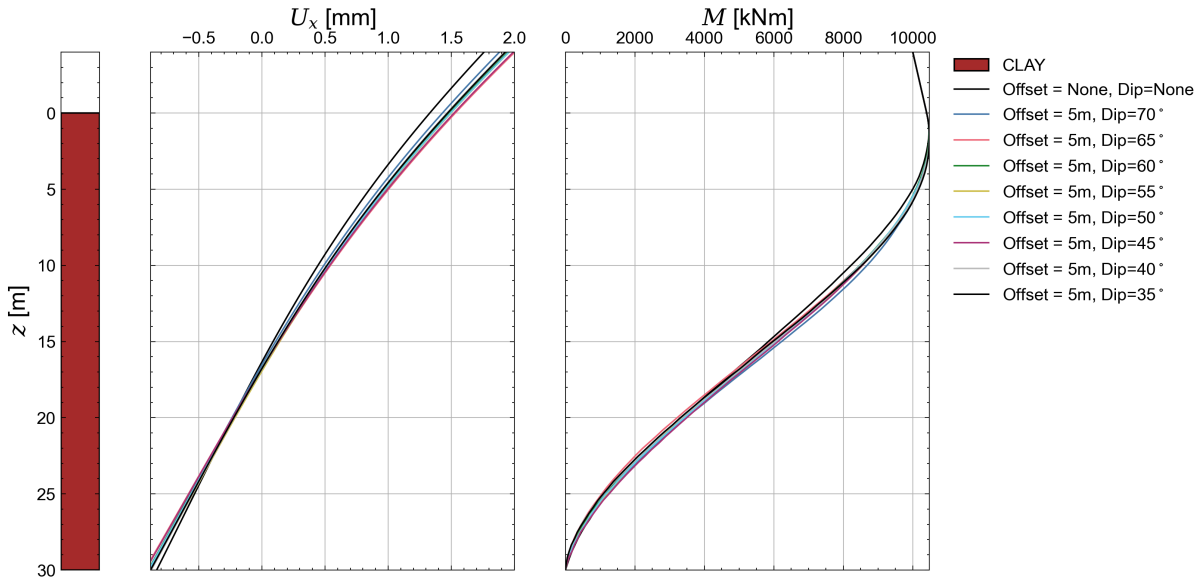

Figure 13: Variation of lateral displacement (U_x) and bending moment (M) with depth for different dips at of the fault (offset = 5 m).

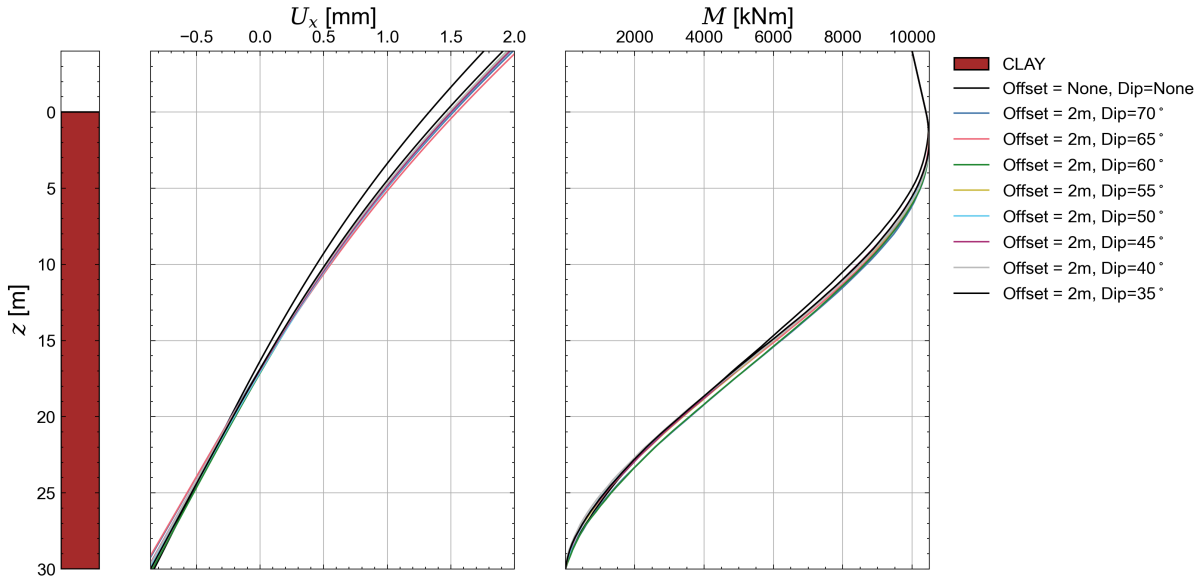

Figure 14: Variation of lateral displacement (U_x) and bending moment (M) with depth for different dips at of the fault (offset = 2 m).

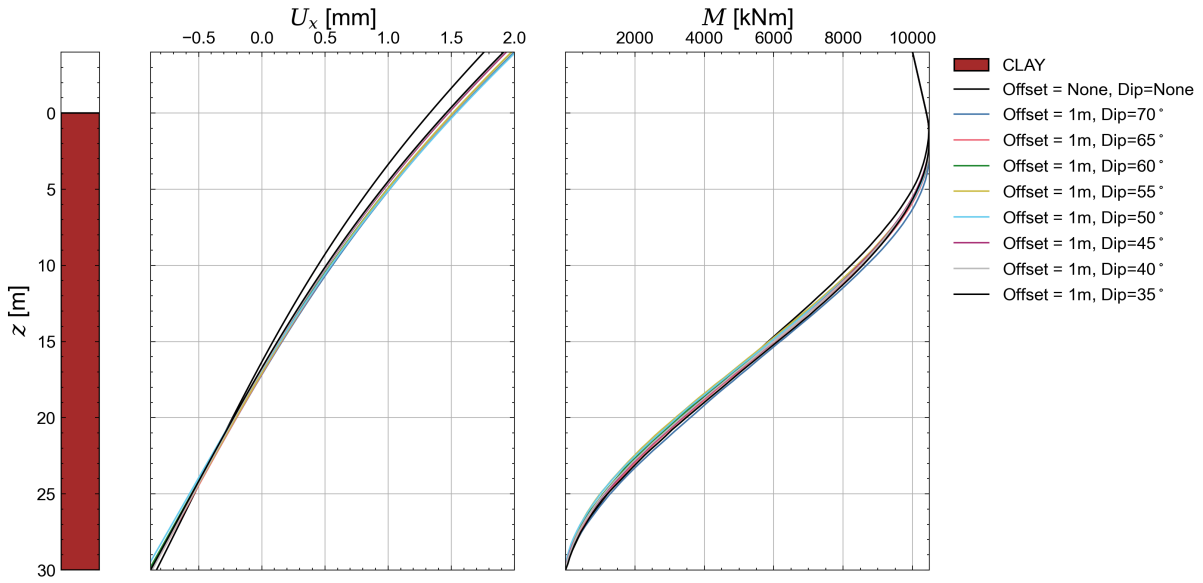

Figure 15: Variation of lateral displacement (U_x) and bending moment (M) with depth for different dips at of the fault (offset =1 m).

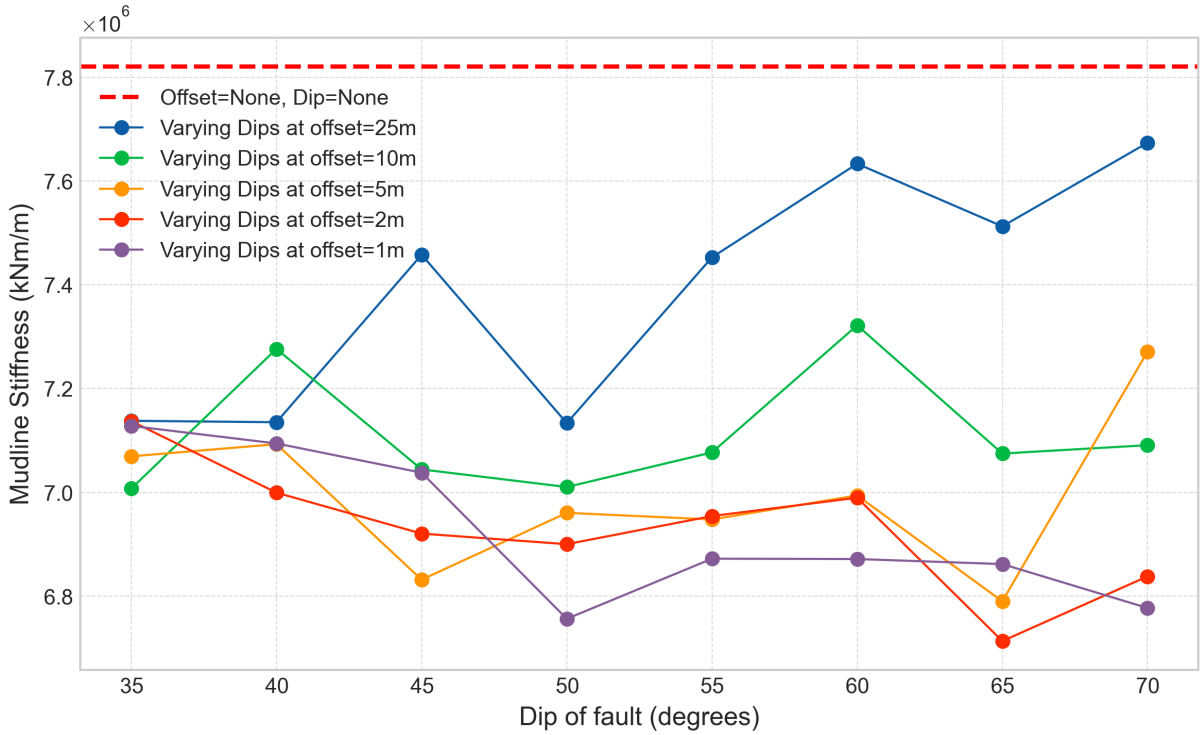

Figure 16: Mudline stifness ($k_{\text{mud}} = M/U_x$)for different offsets of the fault (Dip = 57°).

Fig. 16 shows a clear and consistent dependence of mudline stiffness on the offset distance between the monopile and the fault. For an offset of 25 m, the mudline stiffness remains relatively close to the intact reference value compared with smaller offsets, indicating a limited influence of the fault at this distance. Across the range of dip angles for this specific offset, a trend is observed in which lower dip angles are associated with

reduced stiffness, with the minimum stiffness occurring at a dip of 35°, identifying this as the critical dip for this offset. In contrast, the highest stiffness is obtained at a dip of 70°.This is because at shallow dip and large offset, there will be more interaction compared to steeper dip and larger offsets. Minor local reductions in stiffness are observed around a dip of 45°, but these variations are insufficient to define a critical dip angle. This is because at shallow dip and large offset, there will be more interaction compared to steeper dip and larger offsets.

At an offset of 10 m, the mudline stiffness is reduced compared to the 25 m case and shows a weaker dependence on dip angle. Slightly higher peak stiffness values occur around dip angles of 40° and 60°; however, these variations are insufficient to define a clear trend.

At offsets of 5 m, 2 m, and 1 m, the mudline stiffness decreases progressively with decreasing offset distance, reaching its lowest value at an offset of 1 m. In addition, the general trend indicates a reduction in stiffness with increasing dip angle. For these small offsets, dip angles in the range of approximately 60°–70° can be considered critical, as they are associated with the lowest stiffness values.

4.3 Effect of Load Orientation

Fig. 17 and 18 show the lateral displacement (U) profiles along the pile depth for different loading orientations, corresponding to offset distances ranging from 10 m to 1 m under in-plane loading conditions. In addition to offset and dip, the monopile response is evaluated under lateral loading applied perpendicular, parallel, and oblique to the geological fault for a given offset and dip. These loading orientations are represented through appropriate combinations of horizontal forces and bending moments (more details in Section 3.3), with perpendicular loading inducing maximum normal interaction with the weak plane, parallel loading minimising such interaction, and oblique loading introduced at 30° and 60°through decomposed force–moment components. The following section discusses the resulting displacement and bending moment (based on Eqs. 1 and Eqs. 2) under these loading orientations.

The results show a systematic influence of loading orientation relative to the fault, with this influence becoming stronger as the monopile approaches the fault. For all offsets, loading perpendicular to the fault (90°) produces the largest lateral displacements and bending moments along the pile. This reflects the maximum normal interaction with the weakness plane, leading to reduced lateral stiffness and increased pile deformation. In contrast, loading parallel to the fault (0°) consistently results in the smallest displacements and moments, as normal stress transfer across the fault is minimized and the soil–pile system remains relatively stiffer.

The oblique loading cases (30° and 60°) exhibit intermediate responses, lying between the parallel and perpendicular cases. As expected, the response magnitude increases progressively from 0° → 30° → 60° → 90°, indicating a gradual increase in effective normal interaction with the fault as the loading direction rotates toward fault-normal.

A clear offset dependency is observed. At an offset of 10 m, differences between loading orientations are noticeable but moderate, indicating partial influence of the fault. At the smallest offset of 1 m, the influence of loading direction is strongest, with perpendicular loading causing the most significant increase in displacement and bending moment, highlighting a critical interaction regime when the pile is located very close to the fault.

Overall, the results demonstrate that both proximity to the fault and loading orientation play a controlling role in monopile response. The most unfavorable condition corresponds to small offsets combined with fault-normal loading, while parallel loading remains the least critical across all offsets.

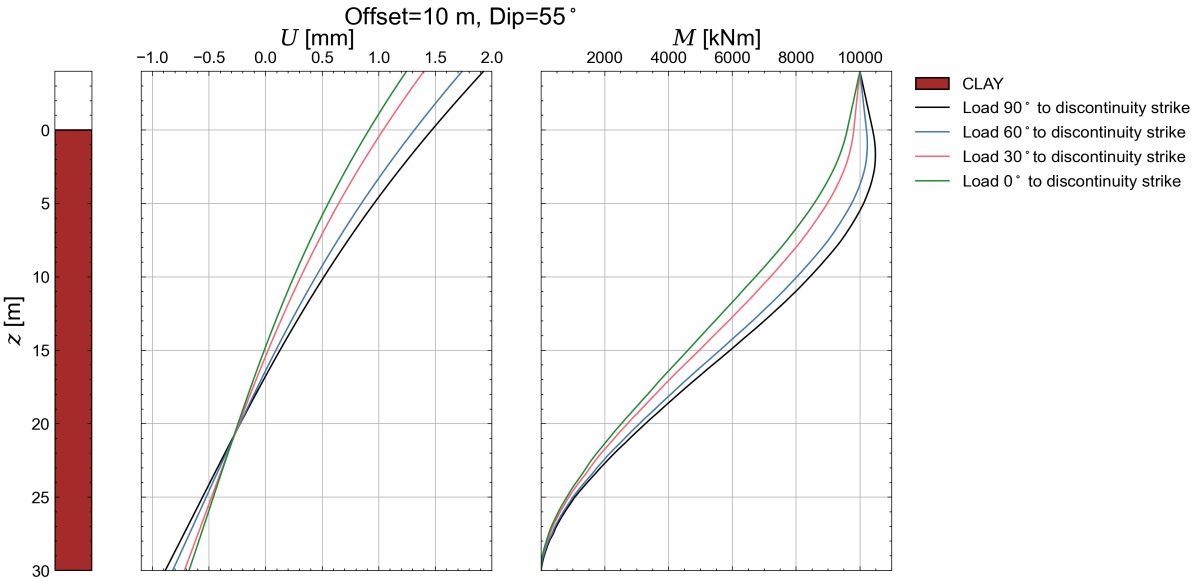

Figure 17: Variation of lateral displacement (U) and Moment with depth for different load orientation at fixed offset = 10 m

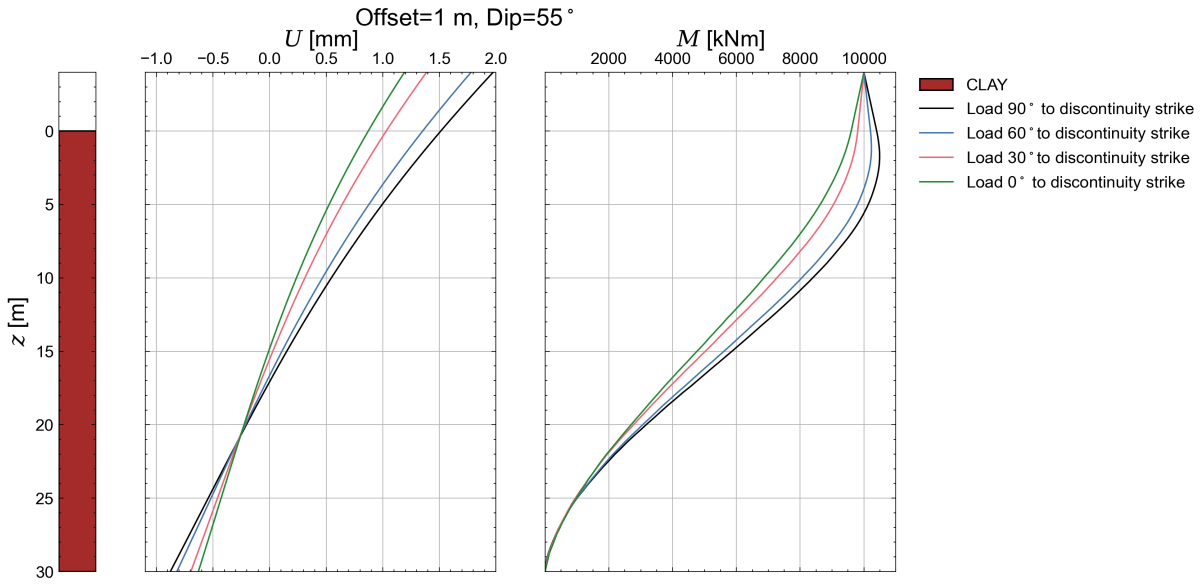

Figure 18: Variation of lateral displacement (U_y) and Moment with depth for different load orientation at fixed offset = 1 m

5 Impact on monopile natural frequency

6 Influence on monopile natural frequency

The analyses indicated a maximum lateral stiffness decrease of 17%. This stiffness decrease can be used in a closed-form solution for the first natural frequency of a monopile-supported wind turbine structure Arany et al. (2015). The wind turbine is modeled by defining the mass of the RNA, the cross-sectional properties of the tower and the cross-section of the monopile. Table 4 shows the monopile and support structure properties used for the analysis. The stiffness coefficients were obtained from a 1D lateral response analysis with PISA response curves (this does not model a fault). The soil properties used for the PISA analysis are given in Table 1.

Table 4: Wind turbine support structure dimensions and masses for closed-form solution (from confidential design documentation)

Property	**Name**	**Value**	**Unit**
Superstructure			
Mass RNA	m_{RNA}	477	Te
Tower mass	m_T	433	Te
Tower length	L_T	86.36	m
Support structure length (top TP to mudline)	L_S	50	m
Tower top diameter	D_t	4.605	m
Tower bottom diameter	D_b	6.5	m
Monopile			
Monopile diameter	D_p	7.8	m
Monopile wall thickness	t_p	66	mm
Young's modulus	E	210.0×10^6	kN/m^2
Stiffness coefficients			
Lateral stiffness	K_L	1.766	GN/m
Lateral/rotational interaction	K_{LR}	-16.967	GN
Rocking stiffness	K_R	334.638	GNm/rad

Two analyses cases were run. In the first, the properties from Table 4 were used to calculate the first natural frequency of the wind turbine structure. A value of 0.2395Hz was obtained. In the second case, the rocking stiffness was reduced by 17%, resulting in a first natural frequency of 0.2317Hz, a percentage reduction of 3.29% compared to the unreduced case. It should be noted that the closed-form solution may result in inaccurate natural frequency estimates, but it does provide an indication of the potential reduction in the first natural frequency due the a fault located immediately next to a monopile.

7 Conclusions

The parametric finite element analyses provide clear evidence of how fault geometry and load alignment influence the performance of offshore monopile foundations. The following main conclusions can be drawn:

1. **Effect of fault offset:** The monopile lateral response is highly sensitive to the distance from the fault. Small offsets between the pile center and the fault strike at the surface of the clay layer (0–10 m) result in pronounced increases in lateral displacement and a significant reduction in mudline stiffness due to reduced con-

finement and direct pile–fault interaction. As the offset increases, the influence of the fault diminishes progressively, and for large offsets (≈25 m) the monopile response converges towards the intact ground condition. The effect is asymmetric, with positive (hanging-wall) offsets exhibiting a stronger influence than negative (footwall) offsets.

2. **Effect of fault dip:** The inclination of the fault governs the severity of the pile–soil interaction, particularly at small offsets. At large offsets, dip angle has only a marginal influence on the monopile response. However, at offsets of 1–5 m, the effect of dip becomes pronounced, with mid- to steep-range dips leading to the greatest reduction in mudline stiffness. For very small offsets, dip angles of approximately 60°–70° are identified as critical, whereas shallower dips tend to redistribute stresses more laterally, resulting in comparatively stiffer behaviour.

3. The influence of loading orientation becomes increasingly pronounced as the monopile approaches the fault, with small offsets (1–2 m) exhibiting a marked separation between loading cases; fault-normal loading results in the largest pile-head displacements and bending moments, indicating a significant reduction in lateral stiffness due to strong normal interaction with the weak plane.

8 Recommendations

Based on the outcomes of the parametric finite element analyses, the following recommendations are made for the design and assessment of offshore monopile foundations in the presence of geological discontinuities:

1. **Consideration of fault proximity in design:** Monopile foundations located within approximately 10 m of a fault should be explicitly analysed considering the presence of the fault. Simplified design approaches assuming intact ground conditions may lead to unconservative estimates of lateral displacement and mudline stiffness for small offsets. For offsets greater than approximately 20–25 m, the influence of the fault becomes negligible, and intact-ground assumptions may be considered acceptable.

2. **Accounting for fault dip effects at small offsets:** For monopiles installed close to a fault (offsets of 1–5 m), the fault dip angle should be treated as a governing parameter in the design. Particular attention should be given to mid- to steeply dipping discontinuities (approximately 60°–70°), which are associated with the most

adverse reductions in mudline stiffness. In such cases, enhanced lateral capacity checks and serviceability criteria are recommended.

3. **Explicit evaluation of loading orientation:** Design load cases should explicitly consider the orientation of lateral loading relative to the fault. Fault-normal loading should be treated as a critical scenario, especially at small offsets, as it results in the largest pile-head displacements and bending moments. Reliance on a single loading direction may underestimate the governing response in fault-affected ground conditions.

4. **Use of advanced numerical modelling for fault-affected sites:** For sites characterised by mapped or inferred geological discontinuities (e.g. glacio-tectonised sediments), three-dimensional numerical modelling is recommended to capture the combined effects of fault offset, dip, and loading orientation. Such models provide a more realistic representation of pile–soil–fault interaction than conventional p–y-based methods.

References

Andikagumi, H., Mestdagh, T., Saritas, H., Plets, R., Missiaen, T., De Batist, M., Stuyts, B., & Pirlet, H. (2025). Faulting in the kortrijk clay formation in the princess elisabeth zone, belgian continental shelf. *VLIZ Special Publication*.

Andikagumi, H., & Batist, M. D. (2025). *Fault geometry and distributions in the princess elisabeth zone, belgian continental shelf* (Report) (Clay Tectonics Project, Deliverable 2.1). Renard Centre of Marine Geology, Department of Geology, Ghent University. Ghent 9000, Belgium.

Arany, L., Bhattacharya, S., Adhikari, S., Hogan, S., & Macdonald, J. H. G. (2015). An analytical model to predict the natural frequency of offshore wind turbines on three-spring flexible foundations using two different beam models. *Soil Dynamics and Earthquake Engineering*, *74*, 40–45.

Fugro. (2024, August). *Geotechnical Parameters Report Volume 3 — Princess Elizabeth Zone, Belgian Continental Shelf* (tech. rep. No. F194660-R-003).

Henriet, J., De Batist, M., Van Vaerenbergh, W., & Verschuren, M. (1988). Seismic facies and clay tectonic features of the ypresian clay in the southern north sea. *Bulletin van de Belgische Vereniging voor Geologie*, *97*, 457–472.

Kallehave, D., Byrne, B. W., LeBlanc Thilsted, C., & Mikkelsen, K. K. (2015). Optimization of monopiles for off-shore wind turbines. *Philosophical Transactions of the Royal Society A: Mathematical, Physical and Engineering Sciences*, *373*(2035), 20140100. https://doi.org/10.1098/rsta.2014.0100

Saritas, H., Mestdagh, T., Andikagumi, H., Plets, R., Missiaen, T., De Batist, M., Stuyts, B., & Pirlet, H. (2025). Pseudo-3d seismic imaging of shallow structural deformations for the development of new windfarms offshore belgium. *86th EAGE Annual Conference & Exhibition*, *2025*(1), 1–5.

Stuyts, B., Devriendt, C., Pirlet, H., Mestdagh, T., Andikagumi, H., & De Batist, M. (2025). Geotechnical characterisation of faulted Paleogene clays. *Proceedings of the 5th International Symposium Frontiers in Offshore Geotechnics*.

WindEurope. (2021, February). Offshore wind in europe – key trends and statistics 2020.

Appendices

A Analysis matrix

Table 5: Design of Experiments for OWT Fault Offset and Loading Scenarios

Exp.	Offset (m)	Dip (°)	F_x (kN)	F_y (kN)	F_z (kN)	M_x (kN·m)	M_y (kN·m)	M_z (kN·m)
0	35	57	100	0	0	0	10000	0
1	25	57	100	0	0	0	10000	0
2	20	57	100	0	0	0	10000	0
3	15	57	100	0	0	0	10000	0
4	10	57	100	0	0	0	10000	0
5	5	57	100	0	0	0	10000	0
6	2	57	100	0	0	0	10000	0
7	1	57	100	0	0	0	10000	0
8	0.1	57	100	0	0	0	10000	0
9	-2	57	100	0	0	0	10000	0
10	-5	57	100	0	0	0	10000	0
11	-10	57	100	0	0	0	10000	0
12	-15	57	100	0	0	0	10000	0
13	-20	57	100	0	0	0	10000	0
14	-25	57	100	0	0	0	10000	0
15	25	70	100	0	0	0	10000	0
16	25	65	100	0	0	0	10000	0
17	25	60	100	0	0	0	10000	0
18	25	55	100	0	0	0	10000	0
19	25	50	100	0	0	0	10000	0
20	25	45	100	0	0	0	10000	0
21	25	40	100	0	0	0	10000	0
22	25	35	100	0	0	0	10000	0
23	10	70	100	0	0	0	10000	0
24	10	65	100	0	0	0	10000	0
25	10	60	100	0	0	0	10000	0
26	10	55	100	0	0	0	10000	0
27	10	50	100	0	0	0	10000	0
28	10	45	100	0	0	0	10000	0
29	10	40	100	0	0	0	10000	0
30	10	35	100	0	0	0	10000	0
31	5	70	100	0	0	0	10000	0
32	5	65	100	0	0	0	10000	0
33	5	60	100	0	0	0	10000	0
34	5	55	100	0	0	0	10000	0
35	5	50	100	0	0	0	10000	0
36	5	45	100	0	0	0	10000	0
37	5	40	100	0	0	0	10000	0
38	5	35	100	0	0	0	10000	0
39	2	70	100	0	0	0	10000	0
40	2	65	100	0	0	0	10000	0
41	2	60	100	0	0	0	10000	0
42	2	55	100	0	0	0	10000	0
43	2	50	100	0	0	0	10000	0
44	2	45	100	0	0	0	10000	0
45	2	40	100	0	0	0	10000	0
46	2	35	100	0	0	0	10000	0
47	1	70	100	0	0	0	10000	0
48	1	65	100	0	0	0	10000	0
49	1	60	100	0	0	0	10000	0
50	1	55	100	0	0	0	10000	0
51	1	50	100	0	0	0	10000	0
52	1	45	100	0	0	0	10000	0

Exp.	Offset (m)	Dip (°)	F_x (kN)	F_y (kN)	F_z (kN)	M_x (kN·m)	M_y (kN·m)	M_z (kN·m)
53	1	40	100	0	0	0	10000	0
54	1	35	100	0	0	0	10000	0
55	35	57	0	100	0	10000	0	0
56	10	70	0	100	0	10000	0	0
57	10	65	0	100	0	10000	0	0
58	10	60	0	100	0	10000	0	0
59	10	55	0	100	0	10000	0	0
60	10	50	0	100	0	10000	0	0
61	10	45	0	100	0	10000	0	0
62	10	40	0	100	0	10000	0	0
63	10	35	0	100	0	10000	0	0
64	5	70	0	100	0	10000	0	0
65	5	65	0	100	0	10000	0	0
66	5	60	0	100	0	10000	0	0
67	5	55	0	100	0	10000	0	0
68	5	50	0	100	0	10000	0	0
69	5	45	0	100	0	10000	0	0
70	5	40	0	100	0	10000	0	0
71	5	35	0	100	0	10000	0	0
72	2	70	0	100	0	10000	0	0
73	2	65	0	100	0	10000	0	0
74	2	60	0	100	0	10000	0	0
75	2	55	0	100	0	10000	0	0
76	2	50	0	100	0	10000	0	0
77	2	45	0	100	0	10000	0	0
78	2	40	0	100	0	10000	0	0
79	2	35	0	100	0	10000	0	0
80	1	70	0	100	0	10000	0	0
81	1	65	0	100	0	10000	0	0
82	1	60	0	100	0	10000	0	0
83	1	55	0	100	0	10000	0	0
84	1	50	0	100	0	10000	0	0
85	1	45	0	100	0	10000	0	0
86	1	40	0	100	0	10000	0	0
87	1	35	0	100	0	10000	0	0
88	35	57	86.6	50	0	5000	8660	0
89	10	70	86.6	50	0	5000	8660	0
90	10	65	86.6	50	0	5000	8660	0
91	10	60	86.6	50	0	5000	8660	0
92	10	55	86.6	50	0	5000	8660	0
93	10	50	86.6	50	0	5000	8660	0
94	10	45	86.6	50	0	5000	8660	0
95	10	40	86.6	50	0	5000	8660	0
96	10	35	86.6	50	0	5000	8660	0
97	5	70	86.6	50	0	5000	8660	0
98	5	65	86.6	50	0	5000	8660	0
99	5	60	86.6	50	0	5000	8660	0
100	5	55	86.6	50	0	5000	8660	0
101	5	50	86.6	50	0	5000	8660	0
102	5	45	86.6	50	0	5000	8660	0
103	5	40	86.6	50	0	5000	8660	0
104	5	35	86.6	50	0	5000	8660	0
105	2	70	86.6	50	0	5000	8660	0
106	2	65	86.6	50	0	5000	8660	0
107	2	60	86.6	50	0	5000	8660	0

Exp.	Offset (m)	Dip (°)	F_x (kN)	F_y (kN)	F_z (kN)	M_x (kN·m)	M_y (kN·m)	M_z (kN·m)
108	2	55	86.6	50	0	5000	8660	0
109	2	50	86.6	50	0	5000	8660	0
110	2	45	86.6	50	0	5000	8660	0
111	2	40	86.6	50	0	5000	8660	0
112	2	35	86.6	50	0	5000	8660	0
113	1	70	86.6	50	0	5000	8660	0
114	1	65	86.6	50	0	5000	8660	0
115	1	60	86.6	50	0	5000	8660	0
116	1	55	86.6	50	0	5000	8660	0
117	1	50	86.6	50	0	5000	8660	0
118	1	45	86.6	50	0	5000	8660	0
119	1	40	86.6	50	0	5000	8660	0
120	1	35	86.6	50	0	5000	8660	0
121	35	57	50	86.6	0	8660	5000	0
122	10	70	50	86.6	0	8660	5000	0
123	10	65	50	86.6	0	8660	5000	0
124	10	60	50	86.6	0	8660	5000	0
125	10	55	50	86.6	0	8660	5000	0
126	10	50	50	86.6	0	8660	5000	0
127	10	45	50	86.6	0	8660	5000	0
128	10	40	50	86.6	0	8660	5000	0
129	10	35	50	86.6	0	8660	5000	0
130	5	70	50	86.6	0	8660	5000	0
131	5	65	50	86.6	0	8660	5000	0
132	5	60	50	86.6	0	8660	5000	0
133	5	55	50	86.6	0	8660	5000	0
134	5	50	50	86.6	0	8660	5000	0
135	5	45	50	86.6	0	8660	5000	0
136	5	40	50	86.6	0	8660	5000	0
137	5	35	50	86.6	0	8660	5000	0
138	2	70	50	86.6	0	8660	5000	0
139	2	65	50	86.6	0	8660	5000	0
140	2	60	50	86.6	0	8660	5000	0
141	2	55	50	86.6	0	8660	5000	0
142	2	50	50	86.6	0	8660	5000	0
143	2	45	50	86.6	0	8660	5000	0
144	2	40	50	86.6	0	8660	5000	0
145	2	35	50	86.6	0	8660	5000	0
146	1	70	50	86.6	0	8660	5000	0
147	1	65	50	86.6	0	8660	5000	0
148	1	60	50	86.6	0	8660	5000	0
149	1	55	50	86.6	0	8660	5000	0
150	1	50	50	86.6	0	8660	5000	0
151	1	45	50	86.6	0	8660	5000	0
152	1	40	50	86.6	0	8660	5000	0
153	1	35	50	86.6	0	8660	5000	0